VOLUME OF FLUID ANALYSIS USING LARGE EDDY SIMULATION ON STANDARD ENGINE COMBUSTION NETWORK INJECTORS

Moaz AL-LEHAIBI [1,*], ***Abdulelah ALHAMAYANI*** [1], ***Brahim MENACER*** [2], ***Víctor TUNINETTI*** [3],
Sunny NARAYAN [4]

[*1]Department of Mechanical engineering, College of Engineering and Architecture, Umm Al-Qura University, P.O. Box 5555, Makkah 24382, Kingdom of Saudi Arabia

[2]Laboratoire des systèmes complexe (LSC), ESGEE Oran, Chemin Vicinal N9, Oran 31000, Algeria

[3]Department of Mechanical Engineering, Universidad de La Frontera, Temuco 4811230, Chile

[4]Department of Mechanics and Advanced Materials, School of Engineering and Sciences, Tecnológico de Monterrey, Av. Eugenio Garza Sada 2501 Sur, Tecnológico, Monterrey 64849, Mexico

[*] Corresponding author: molehaibi@uqu.edu.sa

Accurate prediction of fuel injection and jet formation under diesel-like conditions requires understanding the coupled thermo-fluid processes inside injector nozzles, including pressure-driven acceleration, viscous losses, cavitation, interfacial dynamics, and convective heat transfer. This study numerically investigates these processes for an oxygenated fuel (OME_3) and a conventional diesel surrogate (n-dodecane) using large-eddy simulations with a Volume-of-Fluid approach and real nozzle geometries from standard ECN Spray A, C, and D injectors. OME_3 exhibits higher liquid density than n-dodecane, resulting in lower exit velocity but greater mass flow and denser near-nozzle jets. The divergent Spray C nozzle promotes inlet separation and cavitation, reducing discharge coefficient and jet core density, whereas convergent nozzles (Spray A and D) yield fuller, attached flows and higher discharge efficiency. Despite geometric differences, both fuels show similar internal pressure distributions, indicating that nozzle design dominates over fuel properties in determining internal hydraulics. From a thermal perspective, OME_3 reaches slightly higher liquid temperatures due to weaker turbulent heat transfer and enhanced viscous heating. Overall, the simulations reveal the combined influence of fuel density, viscosity, and nozzle geometry on discharge characteristics, jet structure, and thermal state, offering physics-based insights for optimizing injector and fuel design in clean, high-efficiency diesel combustion systems.

Keywords*: Combustion Network, CFD, Spray A, Spray C, Spray D, projected density, rate of flow, n-dodecane* OME_3

1. Introduction

In recent decades, progressively stricter emission regulations have dramatically lowered vehicle pollutant emissions and driven improvements in engine efficiency [1,2]. At the same time, there is growing interest in oxymethylene dimethyl ether fuels (OME_n, where n indicates the number of $–OCH_2–$ units) as alternatives or supplements to diesel in direct-injection engines [3–5]. One reason is that OMEs can substantially mitigate the typical NOx–soot trade-off in diesel combustion. Notably, OMEs contain no carbon–carbon bonds and have high oxygen content, so they generate very little soot even under diesel engine conditions. This means using OMEn as fuel can potentially resolve the long-standing dilemma of simultaneously reducing soot and nitrogen oxides in engine exhaust [6].

Advances in production technology have also started to lower the cost of OMEn fuels, improving their economic viability [7]. In recent years, novel synthesis routes (for example, from methanol or sustainable feedstocks) have scaled up, making OMEs more affordable and available. As a result, these alternative fuels are becoming increasingly practical options in the marketplace alongside conventional diesel.

Within the OME fuel family, short-chain variants (such as OME_1 and OME_2) pose practical drawbacks like very high volatility and low viscosity. OME_1, for instance, has extremely low viscosity and poor lubricity, which can damage fuel pumps or injectors in unmodified common-rail systems. Using such highly volatile OMEs may require significant engine hardware modifications to prevent fuel delivery problems. In contrast, medium-length OMEs (e.g. OME_3–OME_5) have physical properties closer to diesel – their viscosity and lubricity are much more acceptable for existing fuel systems. Thus, longer-chain OMEs are considered “drop-in” capable synthetic fuels that could be used in current diesel infrastructure without major investments or redesign. Figure 1 illustrates variation of various fuel properties in n-dodecane diesel and representative OMEs.

Research into OMEn fuels has greatly intensified in recent years, as many studies explore their performance in diesel engines. For example, one experimental study compared the combustion of $OME_{3–5}$ blends against conventional diesel in a single-cylinder engine [8]. It found that switching to OME-based fuel dramatically lowers NOx emissions, albeit with a slight reduction in engine thermal efficiency. In a related vein, Pastor et al. [9] examined the flame structure of an OME_3 spray versus an n-dodecane spray under standard ECN “Spray A” conditions using optical analysis. They observed that the OME_3 flame had a somewhat better length of lift-off with s smaller length of flame as compared to n-dodecane. These differences in ignition and flame structure underscore the importance of understanding fuel spray, combustion and emissions behavior.

Further investigations have combined experiments and simulations to characterize OME spray combustion. In one study, neat OME_3 and OME_5 fuels were tested in a constant-pressure spray vessel, and the OME_5 fuel showed an earlier ignition timing compared to diesel [10]. Wiesmann et al. [11] extended this by simulating the spray combustion of an $OME_{3–5}$ blend versus n-dodecane using both Reynolds Navier–Stokes (RANS) and large-eddy simulations (LES). They reported that both RANS and LES were able to capture the behavior of OME fuel sprays accurately, which is encouraging for predictive modeling. To provide a standardized context for such comparisons, the Engine Combustion Network (ECN) defines several canonical injector conditions named Spray A, B, C, and D, which differ in nozzle diameter and internal [12,13]. Table 1 summarizes key specifications of these reference diesel injectors.

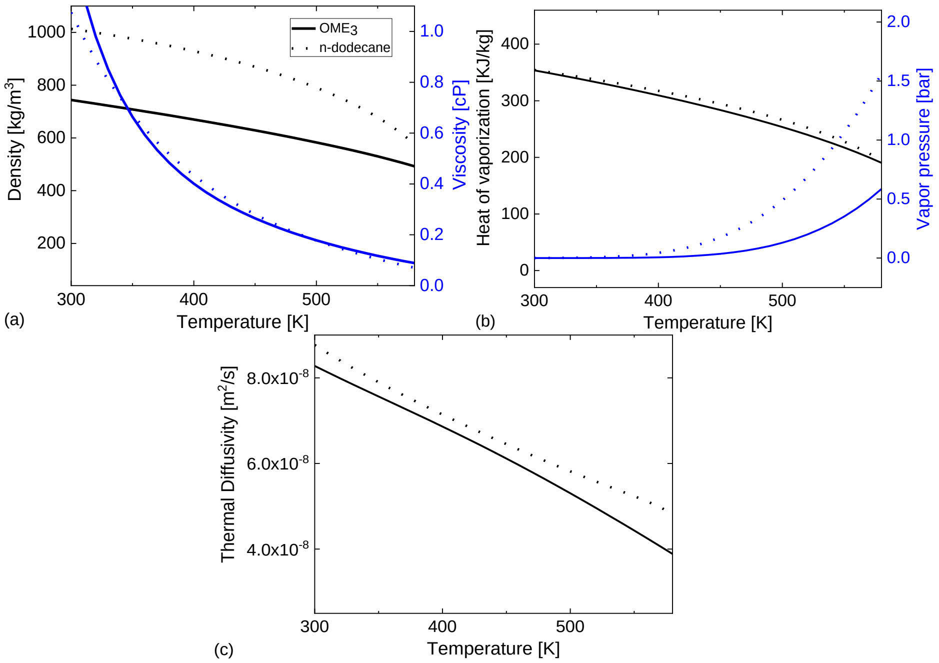

Figure 1: Features of n-dodecane and OME3.

Table 1: ECN Injector Nozzle Specifications.

Spray Type	Serial#	K factor	Diameter (μm)
A	210677	1.5	84
C	210037	-2, -1 [8]	208
D	209134	1.5	191

Each ECN spray target has a nozzle with a specified diameter and K-factor (convergence or divergence of the orifice). Spray A's nozzle is a small 90 μm orifice with a convergent K ≈ +1.5; Spray C's is a much larger 208 μm orifice but divergent (K ≈ –2); Spray D's nozzle is about 190 μm with a strong convergent K ≈ +1.5. Thus, the hole diameters span roughly 0.09–0.20 mm across these standard injectors. The different nozzle sizes and shapes lead to different fuel flow characteristics, which will be explored in the simulations.

To date, there have been very few studies directly comparing the transient spray behaviors of OME fuels and conventional diesel across different injector types using high-fidelity computational models. The present study addresses this gap. In the following sections, we first describe our computational setup, then compare the simulated spray profiles of n-dodecane and OME_3 for the various ECN injectors, and finally discuss the implications for engine combustion.

2. Experimental setup

2.1. ECN

We utilized detailed experimental data from the ECN and Argonne National Lab to inform and validate our simulations. In particular, computed tomography was performed at Argonne to precisely measure the nozzle geometry of the Spray A, C, and D injectors [11–13]. Additional validation data for the injection and flow behavior were obtained from prior experimental works [14–17]. Studies [18–20] provided further context on nozzle-to-nozzle variation and X-ray absorption measurements relevant to our model calibration. We imported these measured nozzle profiles into our Eulerian simulation grid to ensure the injector flow passages were represented realistically. Experimental injection-characterization data were also used for validation; for example, the fuel mass flow rate and spray density measurements for each injector were compared against our simulation predictions to gauge the accuracy of the computational model.

We also incorporated fuel distribution data obtained from X-ray radiography experiments. This technique has been used previously to measure 3D mass distribution, as demonstrated by Kastengren et al. [21]. These experiments measured the fuel's projected density (line-of-sight fuel concentration) in the near-nozzle region for the Spray A, C, and D injectors. Measurements were taken at several axial distances downstream of the nozzle, under nominally steady injection conditions. Because real injector orifices can have asymmetries from manufacturing (leading to slight irregularities in flow), the radiographic density was captured on XY and XZ planes for each spray. As seen in Figure 2 the XY plane is taken when $\theta = 0$ and XZ plane is at $\theta = 90$.. This provided a more complete picture of the spray's cross-sectional density and ensured that any non-symmetric spray features were recorded. These planar density profiles serve as a validation dataset for the simulated fuel distribution immediately outside the nozzle.

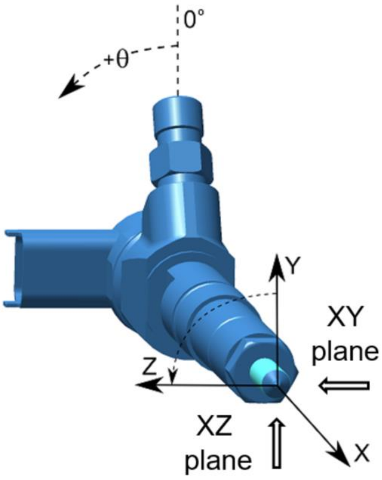

***Figure 2: Schematic defin*ing the orientation of the orifices**

Previous research [22] has indicated that injector-to-injector variability in Spray A nozzles is relatively minor in terms of mass flow rate characteristics. Therefore, for our validation we focused on one representative Spray A injector (serial #210677) and used its measured mass flow curve as the reference. On the other hand, to account for cavitation effects in the larger nozzles, we drew data from Payri et al. [23] for flow in Spray C and D injectors under Spray A-like conditions (same injection pressure and duration). Those measurements showed how cavitation in divergent nozzles (like Spray C) can reduce effective mass flow. Using these experimental insights, we ensure our model captures both the nominal flow rate and the cavitation-induced flow reductions for each injector, which is important for accurately predicting spray development.

2.2. Computational models

The injector geometry is a critical factor influencing the spray's development – it affects the fuel injection velocity, spray angle, and even the rate at which the liquid jet breaks up into droplets [24]. Small geometric details (such as the orifice inlet radius or surface roughness) can measurably alter the flow. For instance, one study found that a rougher-than-expected internal surface can cause the simulations to over-predict mass flow by around 10% if not accounted for [25,26]. To avoid such errors, we used the scanned real geometries of the Spray A, C, and D nozzles in our models rather than idealized geometries. By directly adopting the actual measured injector dimensions and surface features, we improved the fidelity of our simulations and ensured that subtleties like manufacturing tolerances were reflected in the computational model.

LES resolves the large-scale turbulent eddies in the flow while modeling the smaller-scale turbulence, allowing us to capture detailed unsteady flow structures within the injector and spray region. This approach is appropriate for flows characterized by high Reynolds numbers where vortex shedding, cavitation, and turbulent mixing play a significant role. A dynamic Smagorinsky-type sub-grid model was applied so that the turbulence dissipation adapts to local flow conditions.

2.2.1. Prediction model of turbulence

The one equation dynamic-structure LES model is as follows:

$$\frac{\partial k}{\partial t} + \underline{u_i}\frac{\partial k}{\partial x_i} = -\tau_{ij}\frac{\underline{\underline{\partial u_i}}}{\partial x_j} - \varepsilon + \frac{\partial}{\partial x_i}\left(\frac{\nu_t}{\sigma_k}\frac{\partial k}{\partial x_i}\right) \qquad (1)$$

In this equation the stress tensors are defined as

$$\tau_{ij} = c_{ij}k \qquad (2)$$

$$T_{ij} = c_{ij}K \qquad (3)$$

$$K = \frac{1}{2}\left(\underline{\widehat{u_\imath u_\imath}} - \underline{\hat{u}_\imath \hat{u}_\imath}\right) \qquad (4)$$

Further, the grid and the test kinetic energies are related as:

$$K = \hat{k} + \frac{1}{2}L_{ii} \qquad (5)$$

Equation 6 was used to relate stress tensors with the subgrid as:

$$L_{ij} = Kc_{ij} - \widehat{kc_{\imath\jmath}} \qquad (6)$$

The sub-grid tensor used was:

$$\tau_{ij} = 2k\left(\frac{L_{ij}}{L_{ii}}\right) \qquad (7)$$

The constants used for the LES model are summarized in Table 2.

Table 2: Constants used for LES simulation.

C_ε(Constant of turbulence)	1
Sub-grid TKE	2

Viscosity constant	0.5
Drop turbulent constant	0.03
Reciprocal TKE Prandtl	1

2.2.2. VOF modeling

The liquid volume fraction (α_l) was represented in terms of mass m and density ρ as:

$$\alpha_l = \frac{\frac{Y_l}{\rho_l}}{\frac{Y_l}{\rho_l}+\frac{Y_g}{\rho_g}} \tag{8}$$

The chemical species conservation equation is given by:

$$\frac{\partial \underline{\rho}\widetilde{Y_k}}{\partial t} + \frac{\partial \underline{\rho}\widetilde{u_\imath}\widetilde{Y_k}}{\partial x_i} = \frac{\partial}{\partial x_i}\left(\underline{\rho} D \frac{\partial \widetilde{Y_k}}{\partial x_i}\right) + \widetilde{S_k} \tag{9}$$

Where Y_k is species mass fraction, D is the coefficient of mass diffusion, and S_k is the evaporation term.

Equation 10 and 11 were used to find cellular mixture density, energy and enthalpy as:

$$\rho = \rho_g \alpha + \rho_l (1-\alpha) \tag{10}$$

$$e_{mix} = \sum_{gas} Y_i e_i + \left(1 - \sum_{gas} Y_i\right) e_{liquid}\ ,\ h_{mix} = e_{mix} + \frac{P}{\rho} \tag{11}$$

Artificial diffusion and dispersion introduced by up-winding and central differencing schemes are avoided using high-resolution interface capturing (HRIC) [27]. Moreover, the HIRC is recommended to prevent the oscillation that arises from using high-order schemes and when solving energy and turbulence equations. Blending upwind and downwind schemes help in balancing stability and interface sharpness. It works by using information from neighboring cells to construct an interpolated curved interface, as shown in Equation 12, with α^n being the face value being interpolated by HIRC. The ability for HRIC scheme to capture the liquid volume fraction is shown Results and discussion section (Figure 13).

$$\alpha^{n+1} = \alpha^n - \frac{\Delta t}{V}\int_A \alpha^n u \cdot dA + \frac{\Delta t}{V}\int_V (\nabla \cdot u)\alpha^n dV \tag{12}$$

2.2.3. Energy Transport Equation

To solve for the temperature fields shown in the results (Figs. 12, 13, 16, and 17), the governing energy conservation equation is solved. This equation is expressed in terms of the mixture energy (e_{mix}), which was defined in Equation (11):

$$\frac{\partial(\rho e_{mix})}{\partial t} + \nabla \cdot \left(u\,(\rho e_{mix} + P)\right) = \nabla \cdot (k_{eff} \nabla T) + S_h \tag{13}$$

In this equation, u is the fluid velocity vector, P is the pressure, and T is the temperature. The term S_h represents volumetric heat source terms, including the viscous heating mentioned in our analysis. The effective thermal conductivity, k_{eff}, is the sum of the laminar thermal conductivity (k) and the turbulent thermal conductivity (k_t), which is derived from the turbulence model. This equation is solved simultaneously with the mass, momentum, and VOF transport equations to provide a complete description of the thermo-fluid field.

2.2.4. Meshing

Figure 3 shows the nozzle geometry simulations for Spray A, C, and D. The seat where the needle stops is in red, and the needle is divided into regions represented by different colors for simulation purposes. Figure 4 shows the meshing for the Spray C injector with a conical shape of upstream and downstream diameters of 8 mm and 15 mm respectively.

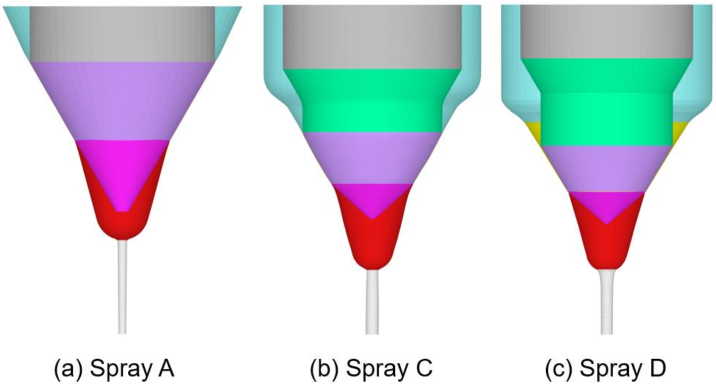

Figure 3: Geometries of nozzles for (a) Spray A (b) Spray C (c) Spray D.

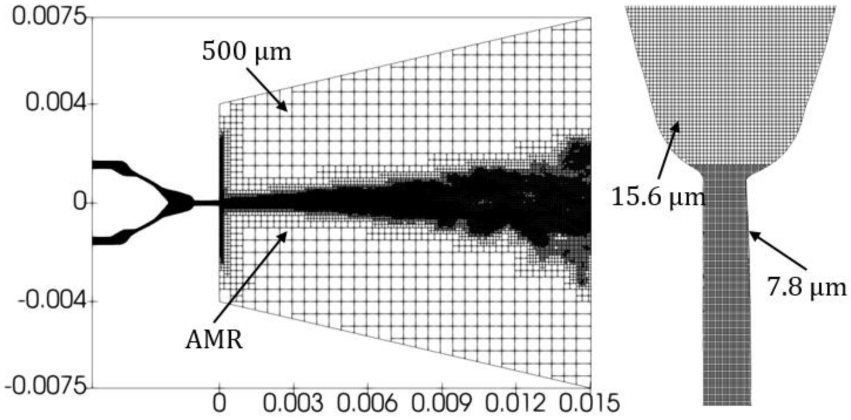

Figure 4: Meshing for Spray C 210037.

The mesh for the flow field is shown in Figure 4 with temperature and pressure 900 K and 60 bars, respectively. Inside the seat the resolution is 15.6 μm whereas in the nozzle it is resolved down to 7.8 μm. In the flow field region, a larger mesh is used with adaptive mesh refinement (AMR). AMR enables the reduction of the simulation time by imposing a condition when the mesh should be refined. The lift profiles, which describe the movement of the needle, were simulated as shown in Figure 5, with nozzle time taken as 400 μs to get a steady state flow. Based on the works of Abers et al. and Yasutomi et al. [28,29], an initial volume fraction of 30% was used for the nozzle sac.

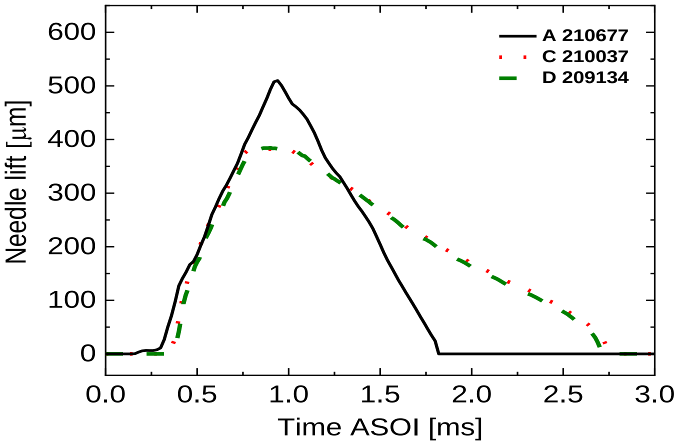

Figure 5: Injector needle lift.

3. Results and discussion

3.1. Density and Rate of flow of sprays

Figure 6 compares the predicted projected densities for n-dodecane and OME3 at 0.1 mm on both the XY and XZ planes using the Spray A injector. The simulation data is extracted at 400 μs after the start of injection (ASOI) when the spray reaches a relatively steady mass flow rate. The experimental data for n-dodecane sprays are also added for model validation. The simulation cases can reasonably reproduce the measured data. The XZ plane tends to induce a more symmetrical distribution of projected density, which trend is well predicted by simulations. Note that OME3 generates a significantly higher peak value than n-dodecane, which is expected due to its higher density.

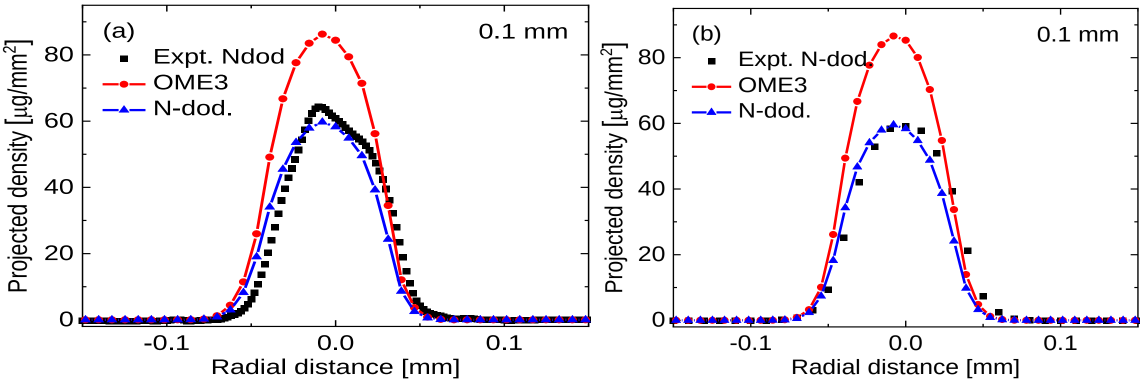

Figure 6: Spray A densities for (a) XY (b) XZ planes.

Figure 7 compares the predicted projected densities for n-dodecane and OME3 at 2.0 mm on both the XY and XZ planes using the Spray C injector. The models can reasonably predict the peak values on the XY and the XZ planes. Note that the Spray C injector demonstrates a more significant impact of the injector orientation on the spray development because of the occurrence of cavitation. A bimodal distribution on the XZ plane is observed. The projected density on the XY plane is consistently higher than the XZ plane for both fuel types. Both fuels show a similar shape, but similar to the Spray A injector, OME3 exhibits the higher projected density for its higher density. Figure 8 compares the predicted projected densities for n-dodecane and OME3 at 2.0 mm on both the XY and XZ planes using the Spray D injector. Since there is no cavitation within the nozzle for the Spray D injector, it yields an overall higher peak projected density than Spray C. Although Spray D also demonstrates an obvious asymmetrical structure on two planes, an unimodal distribution is observed, unlike the Spray C injector.

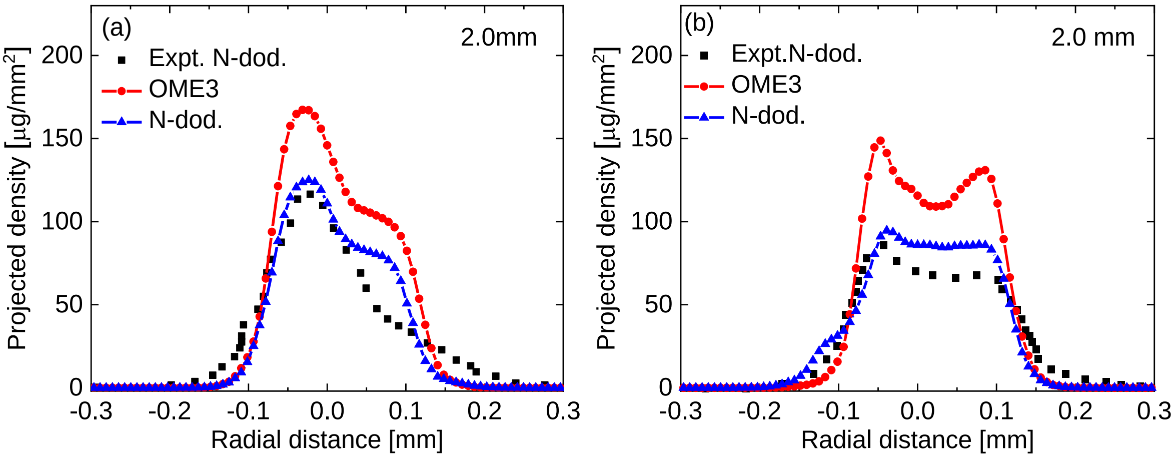

Figure 7: Densities for Spray C (a) XY (b) XZ planes.

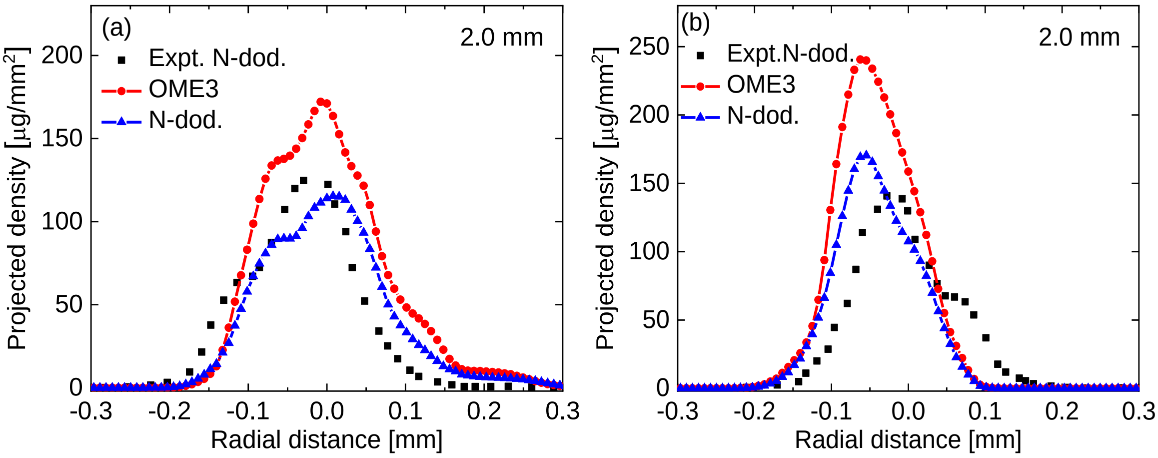

Figure 8: Densities for Spray D on the (a) XY and (b) XZ planes.

Figure 9 compares the predicted projected densities for n-dodecane and OME3 on the XY and XZ planes using three injectors. The effect of the k-factor can be studied by comparing Spray D to C, for which the latter case induces noticeable cavitation and thus a lower projected density. Moreover, the effect of different diameters can be studied by comparing Spray D to A, for which the injectors have the same k-factor. Because of the larger nozzle diameters for Spray C and D than Spray A, their projected densities using both fuels are significantly higher. Note that the projected density on the XY plane for Spray D using OME3 is 56 μg/mm2 higher than n-dodecane. On the other hand, Spray C generates a difference of 44 μg/mm2 when using both fuels due to cavitation. Generally, the XY plane-projected density for OME3 increases in magnitude while preserving the overall shape. Specifically, the bimodal shape is further enhanced on the XZ plane for Spray C when using OME3.

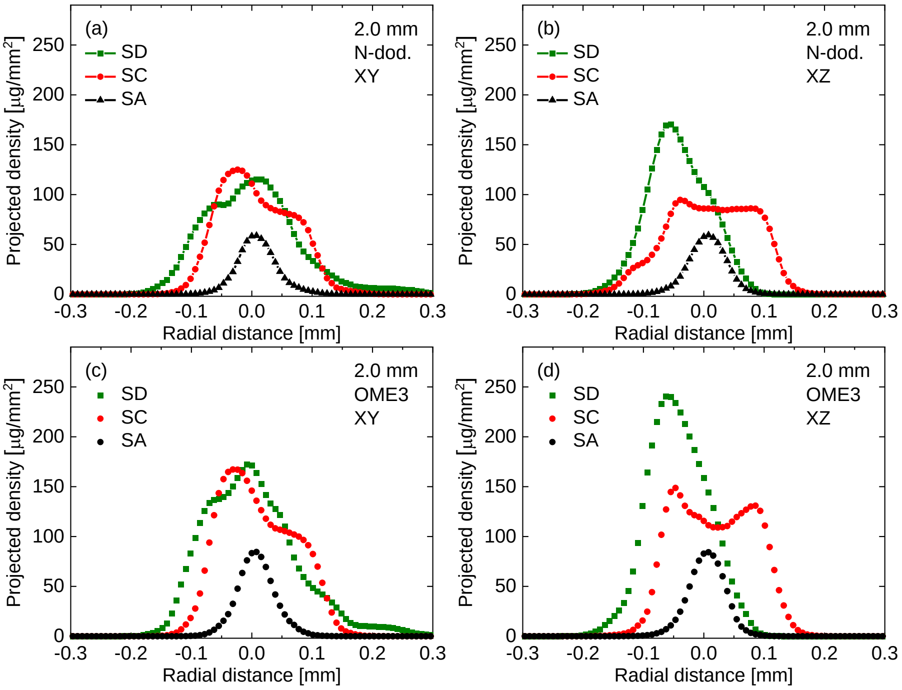

Figure 9: Densities for (a) XY (b) XZ planes, for n-dodecane and (c) XY (d) XZ planes for OME$_3$.

3.2. Flow parameters

The capability of the computational models in reproducing the n-dodecane experiment can be further evidenced by Figure 10, which compares the predicted profiles of mass flow rate and average velocity using three injectors fueled with n-dodecane and OME3. An overall good agreement between the predicted and measured mass flow rates is observed. Comparatively, the steady mass flow rates for Spray A, C, and D are higher for OME3 than n-dodecane by 0.5, 2.1, and 2.4 g/s, respectively. However, the lower predicted velocity is observed for OME3 owing to the higher density and thus the larger mass inertia.

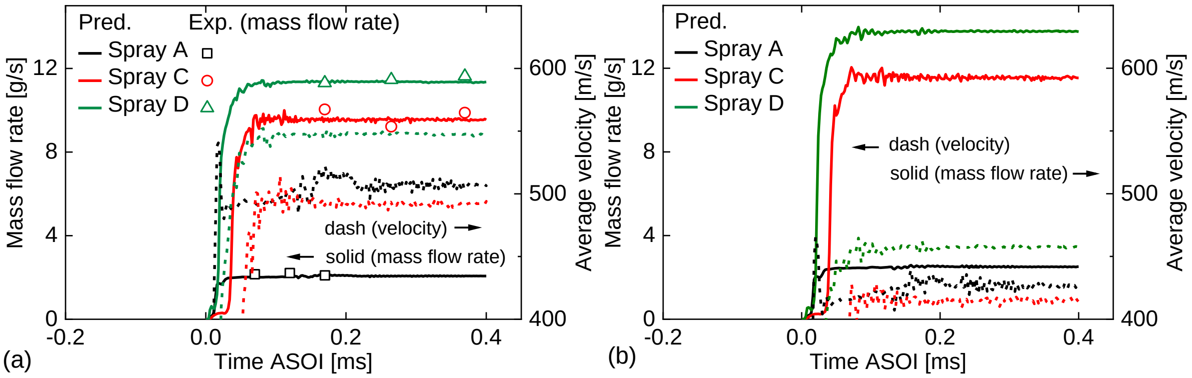

Figure 10: Mass flow rate and average velocity profiles.

Figure 11 compares the predicted axial velocity and turbulent kinetic energy (TKE) using three injectors fueled with n-dodecane and OME3. The x-axis is normalized by the channel length. Note that the right direction is towards the nozzle exit. Both fuels demonstrate a similar trend when using various injectors. However, the velocity fueled with OME3 is significantly lower than n-dodecane due to its higher density and inertia. By comparing the two converging nozzles (i.e., Spray A and Spray D), it is found that regardless of the nozzle size, the internal flow follows a similar gradually accelerating feature, which reaches a peak velocity at the nozzle exit. However, cavitation is generated because of the divergent internal nozzle geometry for the Spray C injector (seen in Figure 3), which has a sharp inlet radius near the sac. It induces an abruptly growing and then gradually decreasing trend of velocity.

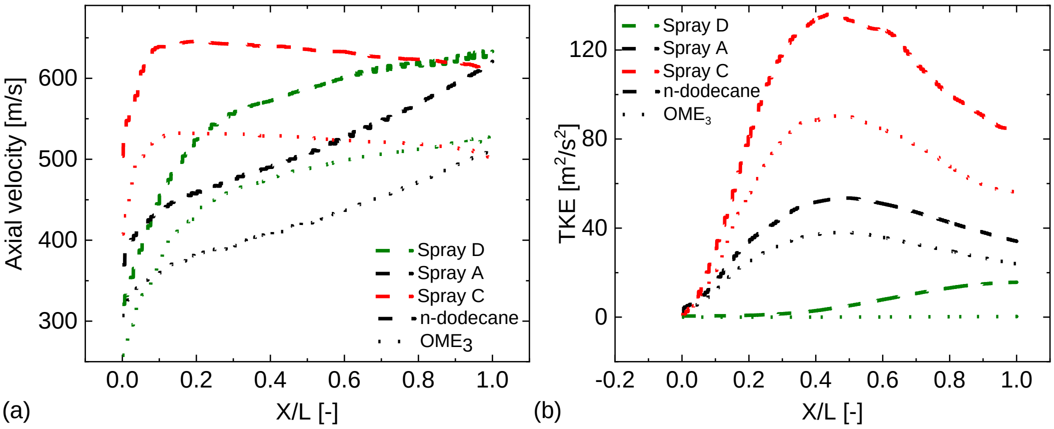

***Figure 11*: *(a) Axial velocity* and *(b) TKE*.**

Figure 12 compares the predicted distributions of gas volume fraction (α_g) and velocity using three injectors fueled with n-dodecane and OME3. As expected, predicted flow fields for these two converging injectors (Spray A and D) depend less on the injector orientation. Both nozzle channels are filled with liquid fuel, indicating no cavitation occurring, which agrees with the previous finding. Moreover, the velocity accelerates as the fluid approaches the nozzle exit, where the pressure is significantly lower than the injection pressure. Note that the OME3 cases lead to an overall lower velocity, but the distribution demonstrates a similar trend with n-dodecane. Obviously, cavitation occurs within the Spray C injector channel, which happens just after the sharp corner, where the velocity gradient is significantly high. Furthermore, different from the other two injectors, obviously distinct flow behaviors are observed in the XY and XZ orientations for the Spray C injector, which will be explained in detail in the next section. Similar to the converging injectors, different fuel properties have a limited effect on the cavitation formation process for the diverging Spray C injector.

Figure 13 compares the predicted distributions of temperature within the channel using the three injectors fueled with n-dodecane and OME3. Although the physical properties of n-dodecane and OME3 are comparable, a slight difference in their density and thermal diffusivity still affects the predicted temperature field. As shown in Figure 13 and Figure 14, OME3 induces a slightly higher temperature distribution than n-dodecane, primarily owing to its lower TKE (seen in Figure 11) and thus the slower heat transfer loss. In addition, the temperature distribution is also affected by the internal nozzle geometry. The results demonstrate that both converging nozzles generate slightly colder core regions, which look nearly axisymmetrical. Comparatively, the temperature evolution within the nozzle channel is significantly more complicated for the diverging Spray C injector. With the growth of the cavity within the nozzle channel of the Spray C injector, the temperature distribution becomes less axisymmetrical. The lower-temperature liquid core moves towards one side, but the other side is instantly filled with the higher-temperature gas.

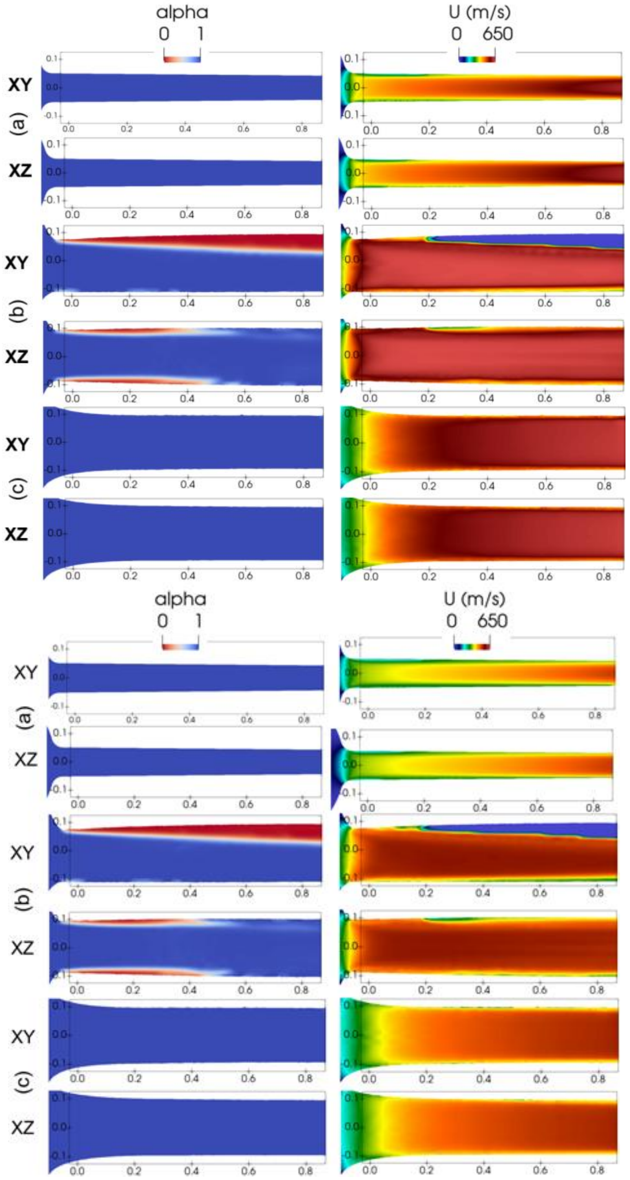

Figure 12: Distributions of gas volume fraction and velocity.

One subtle difference observed between the OME_3 and n-dodecane simulations is the fluid temperature in the nozzle and near-nozzle region, as shown in Figure 13. The OME_3 cases exhibited slightly higher fuel temperatures within the nozzle compared to n-dodecane, which correlates with the lower turbulent kinetic energy observed in Figure 11(b). This is attributed to reduced turbulent mixing and cooling for the OME_3 fuel. Because OME_3 has a higher density and viscosity, the turbulence intensity in the fuel jet is lower, slowing the convective heat transfer from the fuel to the surrounding cooler ambient gas. Consequently, the OME_3 jet retains heat slightly more than the n-dodecane jet. However, this temperature difference is modest—the peak temperature rise in OME_3 was only marginally above that of n-dodecane in the same injector. This observation also aligns with the lower flow velocity predicted for OME_3 in Figure 10, which results in less convective heat removal.

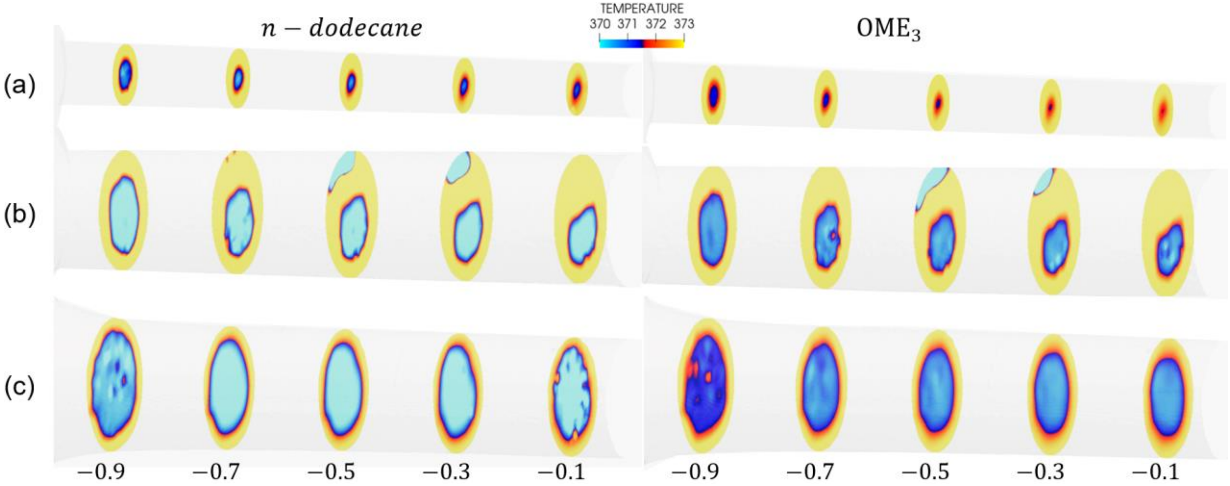

Figure 13: Temperature distributions.

Despite the differences in fuel properties, the simulations show that the overall internal pressure distribution in the injector remains nearly identical for both fuels, as seen in Figure 14. The corresponding density profiles in Figure 15 further confirm that the pressure drop from inlet to exit is governed mainly by nozzle geometry rather than fuel type. For instance, the Spray C nozzle (divergent geometry) shows a more pronounced local pressure drop compared to the convergent Spray A and D nozzles, consistent with the cavitation regions identified in Figure 12. This indicates that the hydrodynamic field inside the injector depends primarily on geometry (K-factor) rather than on the physical differences between OME_3 and n-dodecane. The main behavioral differences, such as inertia and mixing, arise after the fuel exits the nozzle, as reflected in the flow and temperature variations shown across Figures 10–15.

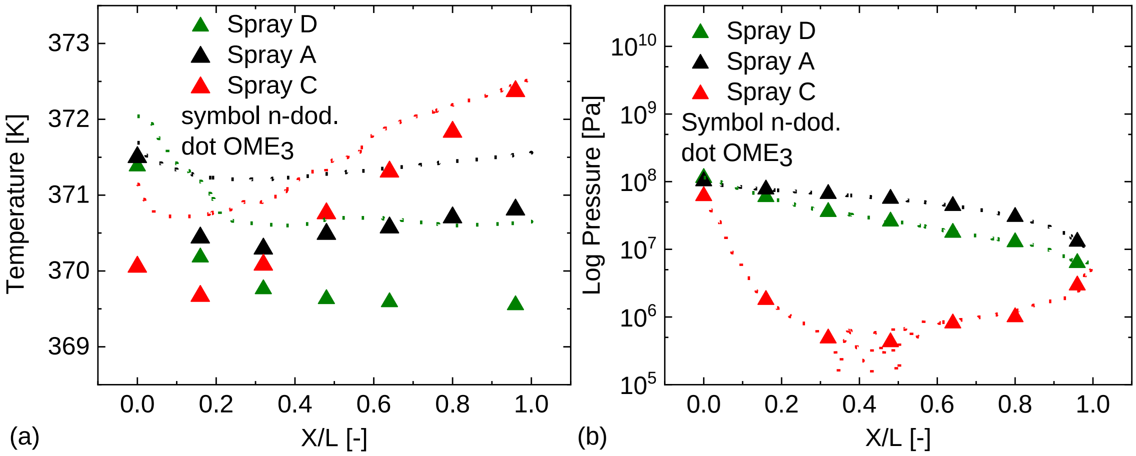

Figure 14: Temperatures and pressure profiles using the three injectors.

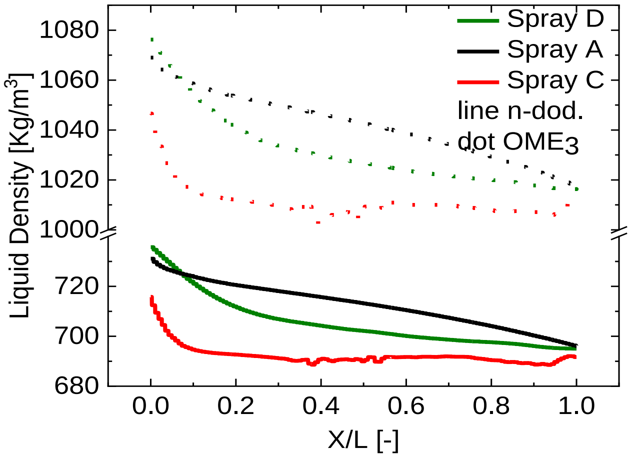

Figure 15: Density profiles using the three injectors fueled.

3.3. Cavitation in spray C

Figure 16 compares the experimental and predicted distributions of gas volume fraction on the XY and XZ planes using the Spray C injector fueled with n-dodecane. The predicted results using the RNG k-Ɛ turbulence model are also added for comparison from previous study [30]. In contrast, the LES simulation yields a more accurate prediction of the cavity occurring within the nozzle channel, regarding size and distribution, especially on the XZ plane. Furthermore, Figure 17 and Figure 18 compare the predicted distributions of gas volume fraction and temperature using the Spray C injector with both fuels on the XY and XZ planes, respectively. As mentioned in the previous section, no apparent difference in the cavity is observed between the two fuels, which could be evidenced by the similar pressure distribution, as shown in Figure 14. The OME3 case induces a slightly higher temperature distribution because of the slower heat transfer process.

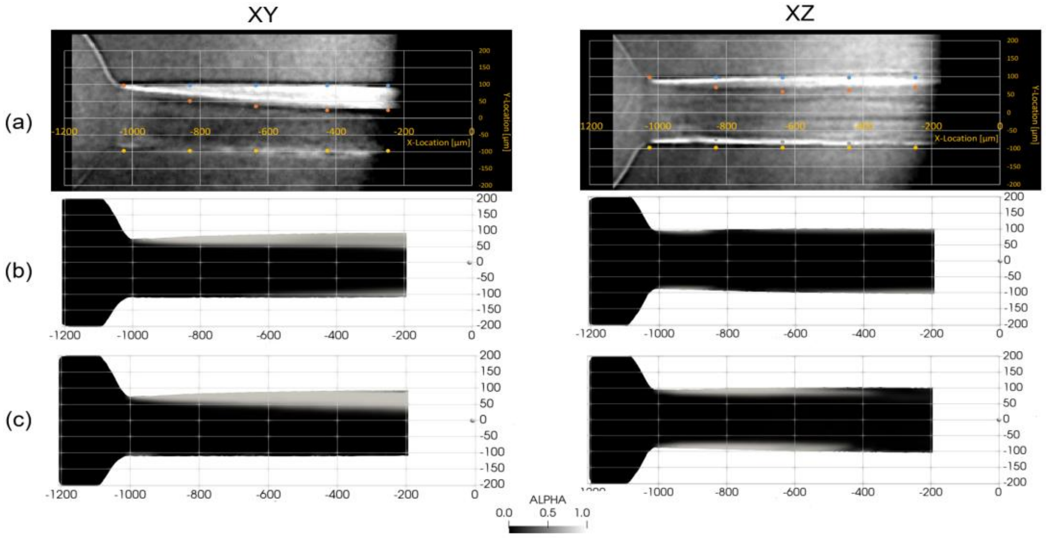

Figure 16: Spray C Gas volume fraction fueled with n-dodecane: (a) Experiment (b) RANS (c) LES.

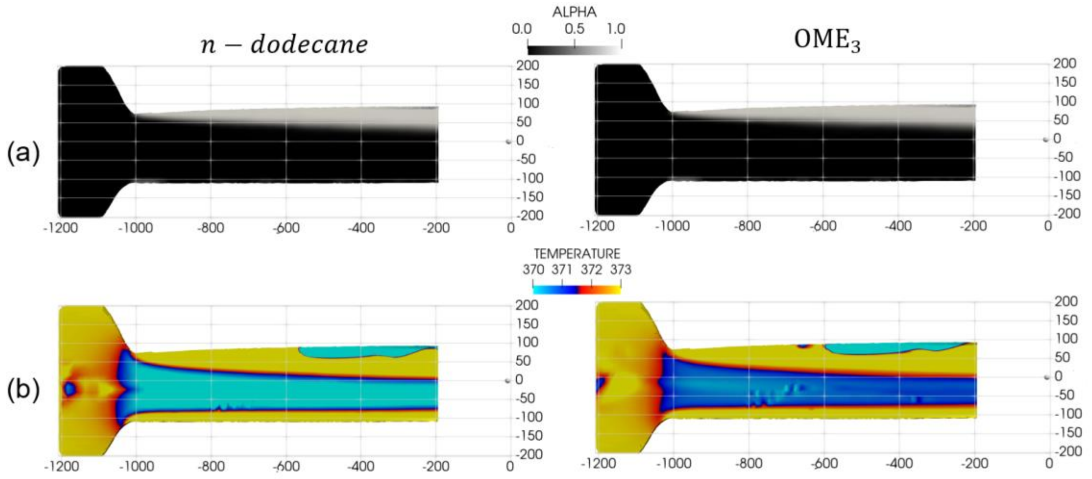

Figure 17: XY plane Gas volume fraction and temperature profile using the Spray C injector: (a)fueled with n-dodecane (b) fueled with OME3.

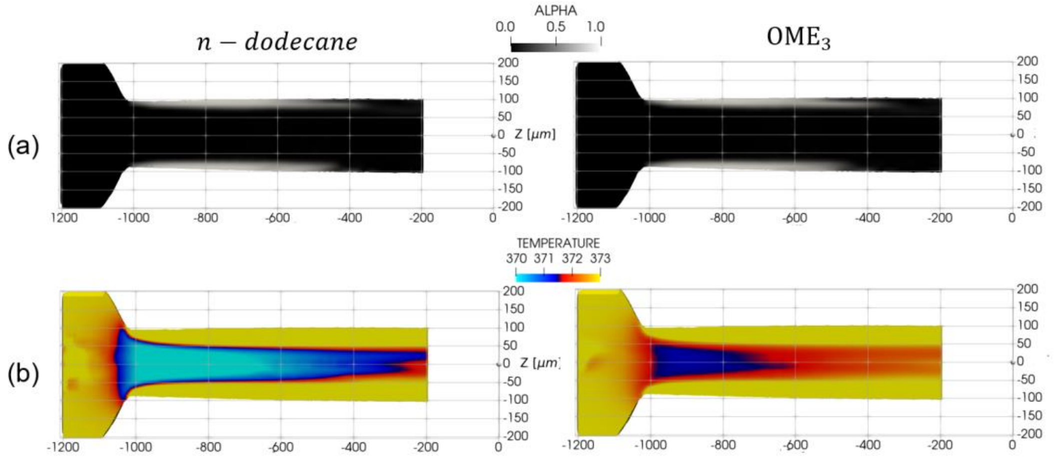

Figure 18: XZ plane Gas volume fraction and temperature distribution with Spray C: (a) fueled with n-dodecane (b) fueled with OME$_3$.

Inside the injector orifices, the flow field analysis highlights the impact of nozzle geometry on cavitation. In the Spray C injector (divergent nozzle), a low-pressure region develops immediately downstream of the orifice inlet. Our LES captures the formation of vapor cavities (cavitation bubbles) along the walls just after the sharp inlet corner in Spray C. This cavitation vapor occupies part of the nozzle cross-section, effectively reducing the liquid flow area and causing the decreased fuel throughput noted above. The Spray D injector, with its convergent inlet, maintains higher pressures along the nozzle wall and shows no significant cavitation in the simulation. Accordingly, Spray D's internal flow remains fully liquid and attached to the walls, supporting a higher mass flow. Spray A's tiny nozzle also showed attached flow without cavitation, but it experiences a much larger pressure drop from inlet to exit due to its small diameter. The cavitation observed in Spray C is important because it can increase turbulence and fuel–air mixing in the near-nozzle region, but it also reduces the fuel flow rate. Our results here align with Payri et al.'s [23] experimental findings, confirming that cavitation in enlarged orifices (like Spray C) leads to flow losses and altered spray development, a phenomenon strongly linked to nozzle geometry [24,31].

4. Conclusions

In summary, this study provided a detailed comparison of OME_3 and n-dodecane fuel sprays using high-fidelity LES simulations with real injector geometries. Key differences were found: OME_3 exhibited a somewhat lower injection velocity (due to higher fuel density) and slightly elevated fuel temperatures in the nozzle (due to reduced turbulent mixing).

Injector geometry proved to have a dominant effect on spray behavior. The convergent nozzles (Spray A and D) delivered higher mass flow, whereas the divergent Spray C suffered flow reduction from cavitation. These findings demonstrate that OME_3 is fluid-dynamically compatible with existing diesel injectors, though its higher density and viscosity lead to distinct flow characteristics. The results also confirm that injector design optimizations (such as avoiding sharp inlets that cavitate) remain crucial for improving spray performance, regardless of the fuel used.

References

[1] Dec, J., A Conceptual Model of DI Diesel Combustion Based on Laser-Sheet Imaging, *SAE transactions*, 106 (1997), pp. 1319-1348.

[2] Walther, S., Li, T., Geyer, D., Dreizler, A., Böhm, B., Soot and Flame Structures in Turbulent Partially Premixed Jet Flames of Pre-Evaporated Diesel Surrogates with Admixture of OMEn, *Fluids*, 9 (2024), 210.

[3] Lautenschütz, L., Oestreich, D., Seidenspinner, P., Arnold, U., Dinjus, E., Sauer, J., Physico-chemical properties and fuel characteristics of oxymethylene dialkyl ethers, *Fuel*, 209 (2017), pp. 812-812.

[4] Virt, M., Zöldy, M., Enhancing the Viability of a Promising E-Fuel: Oxymethylene Ether–Decanol Mixtures, *Energies*, 17 (2024), 1348.

[5] Wiesmann, F., Strauß, L., Rieß, S., Manin, J., Wan, K., Lauer, T., Numerical and Experimental Investigations on the Ignition Behavior of OME, *Energies*, 15 (2022), 6855.

[6] Dworschak, P., Berger, V., Härtl, M., Wachtmeister, G., Neat Oxymethylene Ethers: Combustion Performance and Emissions of OME 2 , OME 3 , OME 4 and OME 5 in a Single-Cylinder Diesel Engine, *SAE Technical Paper 2020-01-0805*, 2020.

[7] Ouda, M., Yarce, G., White, R. J., Hadrich, M., Himmel, D., Schaadt, A., Klein, H., Jacob, E., Krossingc, I., Poly(oxymethylene) dimethyl ether synthesis – a combined chemical equilibrium investigation towards an increasingly efficient and potentially sustainable synthetic route, *Reaction Chemistry & Engineering*, 2 (2017), 1, pp. 50-59.

[8] Rodríguez-Vallejo, D. F., Valente, A., Guillén-Gosálbez, G., Chachuat, B., Economic and life-cycle assessment of OME3–5 as transport fuel: a comparison of production pathways, *Sustainable Energy & Fuels*, 5 (2021), 9, pp. 2504-2516.

[9] Pastor, J., Garcia-Oliver, J., Micó, C., Tejada, F., Comparison of the Diffusive Flame Structure for Dodecane and OME X Fuels for Conditions of Spray A of the ECN, *SAE International Journal of Advances and Current Practices in Mobility*, 3 (2021), 1, pp. 402-411.

[10] Haspel, P., Gierth, S., Popp, S., Scholtissek, A., Rieß, S., Wensing, M., Hasse, C., Large eddy simulation of OME3 and OME4 spray combustion under heavy-duty conditions, *Fuel*, 353 (2023), 129097.

[11] Wiesmann, F., Nguyen, T. M., Manin, J., Pickett, L. M., Wan, K., Tagliante, F., Lauer, T., LES and RANS Spray Combustion Analysis of OME3-5 and n-Dodecane, *Energies*, 17 (2024), 2265.

[12] ***, ECN Diesel Spray Combustion: Target Condition Spray A/B, https://ecn.sandia.gov/diesel-spray-combustion/target-condition/spray-ab/

[13] Du, C., Andersson, M., Andersson, S., Effects of Nozzle Geometry on the Characteristics of an Evaporating Diesel Spray, *SAE International Journal of Fuels and Lubricants,* 9 (2016), 3, pp. 493-513.

[14] Pastor, J. V., García-Oliver, J. M., Micó, C., García-Carrero, A. A., An experimental study with renewable fuels using ECN Spray A and D nozzles, *International Journal of Engine Research*, 23 (2022), 10, pp. 1748-1759.

[15] Yang, S., Yi, P., Habchi, C., Real-fluid injection modeling and LES simulation of the ECN Spray A injector using a fully compressible two-phase flow approach, *International Journal of Multiphase Flow*, 122 (2020), 103145.

[16] Chung, W. T., Ma, P. C., Ihme, M., Examination of diesel spray combustion in supercritical ambient fluid using large-eddy simulations, *International Journal of Engine Research*, 21 (2020), 1, pp. 122-133.

[17] Holzer, A., Günthner, M., Jung, P., Performance of pure OME and various HVO–OME fuel blends as alternative fuels for a diesel engine, Automot. Engine Technol., 7 (2022), pp. 369-383.

[18] Singh, S., Ailaboina, A., Battistoni, M., Danish, M., Saha, K., Numerical Investigation of Cavitation Behavior for Dodecane and OME3 Fuel in ECN Spray C Injector Nozzle, *Proceedings of the 1st International Conference on Fluid, Thermal and Energy Systems (ICFTES 2022), Lecture Notes in Mechanical Engineering*, Springer, Singapore, 2024.

[19] ***, Engine Combustion Network, https://ecn.sandia.gov/

[20] Powell, C., Ciatti, S., Cheong, S., Liu, J., X-Ray absorption measurements of diesel sprays and the effects of nozzle geometry, *SAE Technical Paper 2004-01-2011*, 2004.

[21] Kastengren, A., Powell, C., Liu, Z., Wang, J., Time Resolved, Three Dimensional Mass Distribution of Diesel Sprays Measured with X-Ray Radiography, *SAE Technical Paper 2009-01-0840*, 2009.

[22] Malbec, L., Egúsquiza, J., Bruneaux, G., Meijer, M., Characterization of a Set of ECN Spray A Injectors: Nozzle to Nozzle Variations and Effect on Spray Characteristics, *SAE International Journal of Engines*, 6 (2013), 3, pp. 1642-1660.

[23] Payri, R., Gimeno, J., Cuisano, J., Arco, J., Hydraulic characterization of diesel engine single-hole injectors, *Fuel*, 180 (2016), pp. 357-366.

[24] Allehaibi, M., Liu, X., Aljabri, H., Ben Houidi, M., Investigation of the Engine Combustion Network Spray C Characteristics at High Temperature and High-Pressure Conditions Using Eulerian Model, *SAE Technical Paper 2021-24-0056*, 2021.

[25] Yue, Z., Battistoni, M., Som, S., Spray characterization for engine combustion network Spray G injector using high-fidelity simulation with detailed injector geometry, *International Journal of Engine Research*, 21 (2020), 1, pp. 226-238.

[26] Richards, K., Senecal, P., Pomraning, E., *CONVERGE (v3.0)*, Convergent Science, Madison, WI, USA, 2021.

[27] Waclawczyk, T., Koronowicz, T., Modeling of the Wave Breaking with CICSAM and HRIC High-Resolution Scheme, *Proceedings of ECCOMAS CFD*, Egmond an Zee, The Netherlands, 2006.

[28] Yasutomi, K., Hwang, J., Manin, J., Pickett, L., Diesel injector elasticity effects on internal nozzle flow, *SAE Technical Paper 2019-01-2284,* 2019.

[29] Abers, P., Cenker, E., Yasutomi, K., Hwang, J., Effect of pressure cycling on gas exchange in a transparent fuel injector*, SAE Technical Paper 2019-01-2280*, 2019.

[30] Allehaibi, M., Liu, X., Aljabri, H., Ben Houidi, M., Mohan, H., Im, H., Investigation of the Engine Combustion Network Spray C Characteristics at High Temperature and High-Pressure Conditions Using Eulerian Model, *SAE Technical Paper 2021-24-0056*, 2021.

[31] Sforzo, B. A., *Fuel nozzle geometry effects on cavitation and spray behavior at diesel engine conditions*, Report No. (SNL-NM), Sandia National Lab., Albuquerque, NM, USA, 2018.

Author Contributions: Conceptualization: M.A. and A.A.; Methodology: M.A.; Software: M.A.; Validation: M.A., V.T. and S.N.; Formal analysis: A.A.; Investigation: M.A.; Resources: B.M.; Data curation: B.M.; Writing – original draft: M.A.; Writing – review & editing: V.T.; Visualization: V.T.; Supervision: B.M.; Project administration: B.M.; Funding acquisition: S.N.

Paper submitted: 16 May 2025
Paper revised: 24 October 2025
Paper accepted: 25 November 2025